PROCEEDINGS OF SPIE

Laboratory simulation of Euclid-like sky images to study the impact of CCD radiation damage on weak gravitational lensing

T. Prod'homme, P. Verhoeve, T. Oosterbroek, N. Boudin, A. Short, et al.

SPIE.

Laboratory simulation of Euclid-like sky images to study the impact of CCD radiation damage on weak gravitational lensing

T. Prod'homme*[a], P. Verhoeve[a], T. Oosterbroek[a], N. Boudin[a], A. Short[a], R. Kohley[b]

[a]European Space Agency, ESTEC, Keplerlaan 1, 2200AG Noordwijk, The Netherlands;
[b]European Space Agency, ESAC, P.O. Box 78, E-28691 Villanueva de la Cañada, Madrid, Spain

ABSTRACT

Euclid is the ESA mission to map the geometry of the dark universe. It uses weak gravitational lensing, which requires the accurate measurement of galaxy shapes over a large area in the sky. Radiation damage in the 36 Charge-Coupled Devices (CCDs) composing the Euclid visible imager focal plane has already been identified as a major contributor to the weak-lensing error budget; radiation-induced charge transfer inefficiency (CTI) distorts the galaxy images and introduces a bias in the galaxy shape measurement. We designed a laboratory experiment to project Euclid-like sky images onto an irradiated Euclid CCD. In this way – and for the first time – we are able to directly assess the effect of CTI on the Euclid weak-lensing measurement free of modelling uncertainties. We present here the experiment concept, setup, and first results. The results of such an experiment provide test data critical to refine models, design and test the Euclid data processing CTI mitigation scheme, and further optimize the Euclid CCD operation.

Keywords: Euclid, CCD, Radiation damage, CTI, Weak lensing, Laboratory experiment

1. INTRODUCTION

Euclid is an ESA medium-class mission designed to unravel the mystery of the accelerating expansion of our universe. It will track the signatures of this expansion and study the growth of structures over the past 10 billion years, using two cosmological probes: baryonic acoustic oscillations and weak gravitational lensing. Weak gravitational lensing is used to map the mass distribution of foreground lensing objects, it requires measuring the shape of the lensed background galaxies with great accuracy, this over a large area in the sky. The Euclid visible imager is designed to perform weak-lensing measurements at an unprecedented accuracy by imaging a 0.55-deg^2 field of view in a single wavelength range 550-920nm with a point spread function (PSF) of 0.18 arcsec FWHM. It is composed of a 6x6 CCD mosaic focal plane, a shutter, and a calibration unit.

Euclid will be launched in 2020 for 6 years of operation at the Sun-Earth Lagrange point 2. During operation the performance of the 36 CCDs will gradually degrade due to radiation damage. In particular the density of defects in the CCD silicon lattice – charge traps – will increase and as so the charge transfer inefficiency (CTI), resulting in a slight but significant distortion of images. Image distortion will introduce errors in the weak-lensing measurement.

So far – in the context of Euclid or a spaceborne weak-lensing dedicated instrument - the effect of CTI on measuring the shape of galaxies was only studied through the mean of modelling. Charge transfer and trapping models are fitted to common CCD characterisation test data (e.g. Extended-Pixel Edge Response, First Pixel Response) obtained in close-to operational conditions to derive representative model parameters that can be subsequently applied to synthetic galaxy and star images. However the model parameters are degenerate and charge trapping is a complex process: stochastic, non-linear with signal level, and highly variable with the CCD illumination history. Modelling, even if indispensible, thus carries uncertainties.

We designed a laboratory experiment to provide a model-free evaluation of the impact of radiation-induced CTI on Euclid galaxy shape measurement. By consecutively projecting a mask pattern on irradiated and reference regions of an irradiated CCD, and comparing the image parameters resulting from the image processing algorithms in each case, we infer the CTI-induced measurement bias. To perform this measurement in controlled conditions and to exclude any potential source of spurious ellipticity we designed a particular mask pattern and specifically irradiated a Euclid CCD prototype. We first present the experiment driving concept and setup. We then detail and discuss a first characterization of the CTI-induced errors in the ellipticity measurement.

*thibaut.prodhomme@esa.int

2. EXPERIMENT SETUP

2.1 Concept

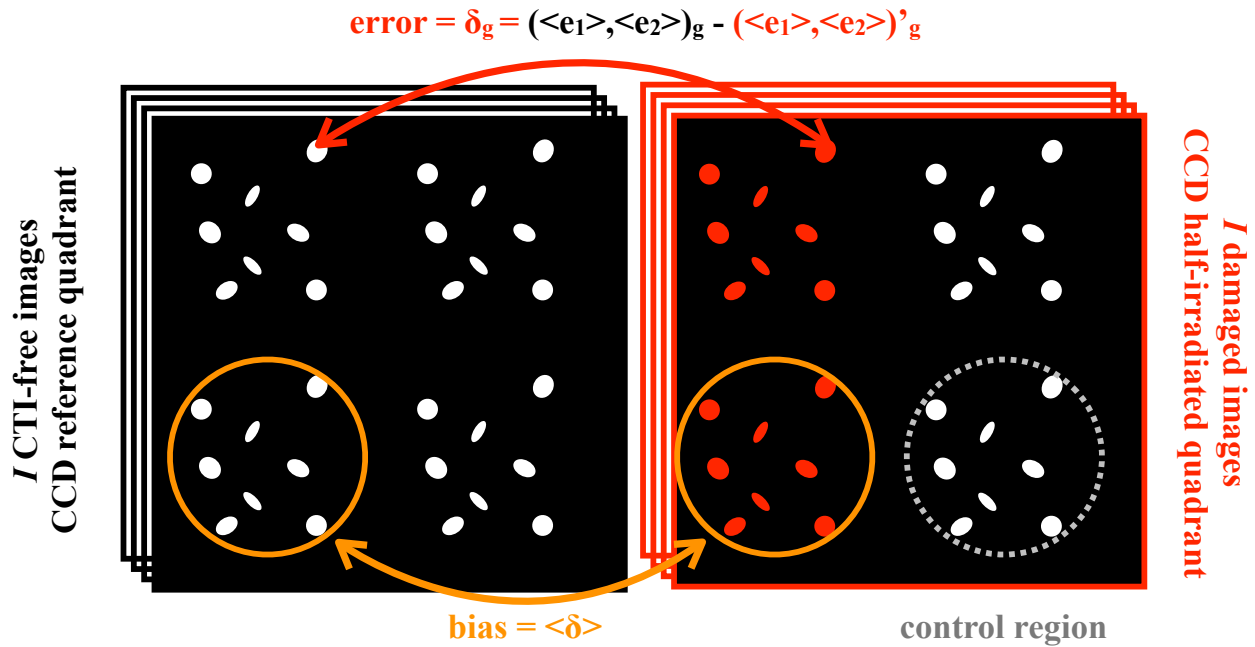$$\text{error} = \delta_g = (<e_1>,<e_2>)_g - (<e_1>,<e_2>)'_g$$

Figure 1. Experiment concept: to measure the CTI-induced error in the shape measurement, we compare the same mask element projected over reference (non-irradiated region, left) and irradiated (right) regions. To obtain the CTI-induced bias we use a subset of elements as comparison unit between images instead of a single element. To check for non-CTI spurious ellipticity potentially affecting our measurement we use the mask elements projected over control regions.
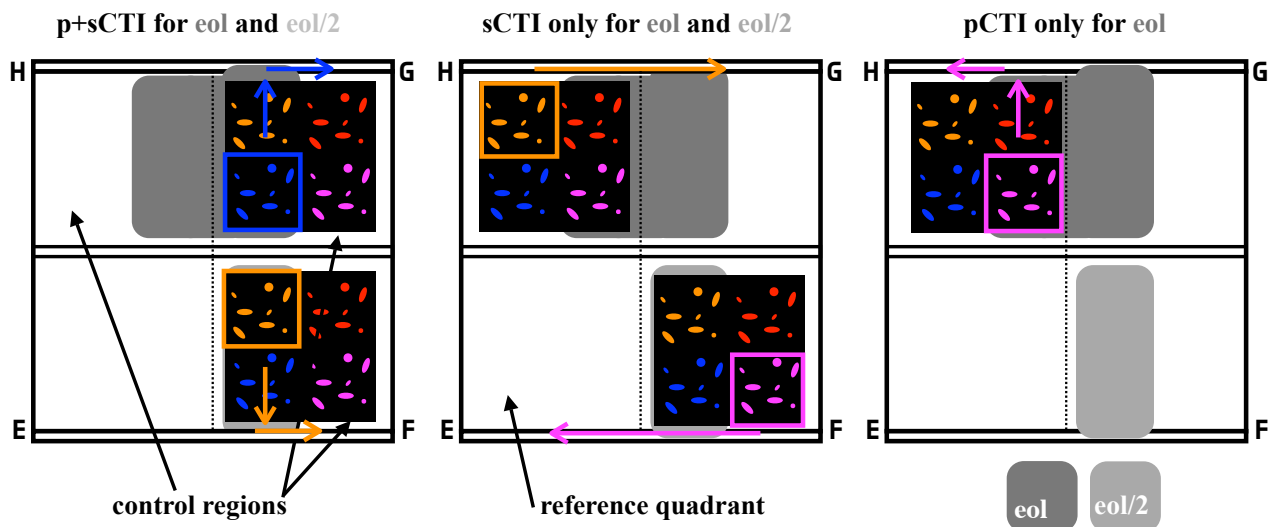

Figure 2. Examples of mask location versus readout configurations that enable disentangling serial from parallel CTI-induced errors in the shape measurement. The CCD and its four quadrants and associated readout nodes (E,F,G,H) are represented as well as the irradiated regions (in grey), the serial registers (top and bottom) and the charge injection structure (middle). Each of the mask sub-patterns (see next Section) is depicted with a different colour.

The goal of this experiment is to measure and characterize errors introduced by radiation-induced CTI in the galaxy shape measurement in conditions as close as possible from the Euclid in-orbit ones. The experiment concept is illustrated in Fig. 1: we first acquire a series of images of the same mask projected over irradiated and reference (non-irradiated) regions of the CCD, and then measure in each image i the ellipticity vector $(e_1, e_2)_{i,g}$ for each of the mask elements (galaxies, g). The error for a particular galaxy g is obtained as follows:

$$\overline{\delta_g} = (\delta_{e1}, \delta_{e2})_g = (\langle e_1 \rangle, \langle e_2 \rangle)_g - (\langle e_1 \rangle, \langle e_2 \rangle)'_g = \frac{1}{I} \sum_i (e_1, e_2)_{i,g} - \frac{1}{I} \sum_i (e_1, e_2)'_{i,g} \qquad (1)$$

with $(\langle e_1 \rangle, \langle e_2 \rangle)_g$, $(\langle e_1 \rangle, \langle e_2 \rangle)'_g$ the mean ellipticity for a galaxy g measured respectively over the I CTI-free images (i.e. obtained over a reference CCD region) and the I damaged images (i.e. obtained over the irradiated CCD region). The CTI-induced error for a particular galaxy g depends on its original shape, orientation, and size. To characterise the CTI-induced errors independently from the galaxy original properties, we compute the CTI-induced bias – the mean CTI-induced errors for a galaxy subset containing G galaxies:

$$\langle \overline{\delta} \rangle = (\langle \delta_{e1} \rangle, \langle \delta_{e2} \rangle) = \frac{1}{IG} \sum_g \sum_i (e_1, e_2)_{i,g} - \frac{1}{IG} \sum_g \sum_i (e_1, e_2)'_{i,g} \qquad (2)$$

The statistical uncertainty on the bias is:

$$\overline{\upsilon_{\langle \delta \rangle}} = \frac{\overline{\sigma_{\langle \delta \rangle}}}{\sqrt{I}} \qquad (3)$$

$$\text{with } \overline{\sigma_{\langle \delta \rangle}} = \sqrt{\overline{\sigma}^2_{(\langle e_1 \rangle \langle e_2 \rangle)} + \overline{\sigma}^2_{(\langle e_1 \rangle \langle e_2 \rangle)'}} \qquad (4)$$

and $\overline{\sigma}_{(\langle e_1 \rangle \langle e_2 \rangle)}$ is the galaxy subset mean ellipticity standard deviation computed over the I images.

The Euclid device comprises four output nodes (cf. [1] and the next sub-section). In combination with a specific irradiation scheme (cf. Fig. 2 and [2]), using a single device we are able to measure errors caused by CTI occurring in the serial and parallel transfer directions independently, and for two different radiation doses.

The measurement concept (Fig. 1) relies on the assumption that the system optical properties over each mask element – the PSF – remains stable over time and after the projection system is displaced from one CCD quadrant to the next. To check for any spurious ellipticity introduced by non-CTI effects, we included large control regions in each of the irradiated quadrant (Fig. 2).

2.2 Tested device characteristics, operation, and irradiation

The tested device is a back-illuminated Euclid prototype CCD 273 with serial number 11263-07-01 custom-made by e2v as part of the Euclid CCD pre-development phase. At the time of writing, it is the most representative device of the future Euclid FM device; changes in the device design and manufacture subsequent to the pre-development phase [1] are expected to have no impact on its CTI performance. The Euclid CCD is a red-enhanced 40 um-thick device comprising an array of 4132×4096 parallel×serial light-sensitive pixels of 12×12 μm size, 4 output nodes, and a charge injection structure along the horizontal direction located at the center of the device. This structure prevents from reading the top image section using the bottom output nodes and inversely, however top and bottom image sections can be read out from either left or right output nodes (as already suggested by Fig. 2).

We operate the CCD in nominal Euclid conditions at a temperature of 153 K and at a readout frequency of 70 kHz. Several optimizations of the clocking scheme and speed are under investigation to reduce parallel and serial CTI, e.g. multi-level clocking of the parallel image clocks [3], increased parallel transfer duration [3,2], even serial register clock width. Only the latter was used during the acquisition of the presented data, in Section 4 the effects of further optimizations are discussed.

The CCD irradiation took place at Kernfysisch Versneller Instituut (Groningen, The Netherlands) in April 2013, it was performed at room temperature using a 38.5 MeV primary proton beam degraded to 10.4 MeV. Using two different shielding masks and irradiation durations, half the bottom left quadrant (readout node F) received a 2.4×10^9 protons cm^{-2} (10 MeV equivalent) fluence and the top right and left quadrant halves (H and G) received a 4.8×10^9 protons cm^{-2} fluence – the Euclid requirement level for end-of-life (eol) solar proton fluence. The charge injection structure, the entire E quadrant, the serial register of the H quadrant, and the four output nodes were not irradiated. Following the irradiation the CCD was stored at room temperature and repeatedly cooled down to 153 K for data acquisition.

We used the ESA Payload Technology Validation section CCD test bench located at ESTEC (Noordwijk, The Netherlands). A comprehensive description of the data acquisition system, driving electronics, temperature and vacuum control system can be found in [4, 5]

2.3 Projected scene properties

The projected mask pattern contains extended sources – galaxies – and point-like sources – stars. The galaxies are used for the main purpose of this experiment: measuring the shape measurement errors introduced by CTI, while the stars are critical to determine and monitor the system PSF at different locations on the CCD. We designed the mask pattern to be as representative as possible of a typical Euclid wide survey scene (see [6, 7]) in terms of object number density, relative locations, shapes and sizes.

The projected scene occupies a CCD quadrant (roughly 2.5x2.5 cm^2), following the Euclid requirements for the 'average number density of galaxies per square arcminute usable for weak lensing' and the 'minimum number of stars per field usable for PSF determination', we derive that the galaxy and star number density should respectively be 360 and 16. We increased the galaxy number to 400 for the sake of statistics, and the star number to 24 for a better area coverage with the PSF determination in mind.

Galaxies and stars are divided up in four identical sub-patterns to preserve the possibility of applying our measurement principle while rotating the mask. The mask rotation provides different scenarios (CCD illumination histories) and can increase some statistics, e.g. how a particular object is affected by CTI as a function of distance to the readout node. For a magnification factor of one, the galaxy sub-patterns are separated by 2048 pixels in both parallel and serial directions. Within each sub-pattern the galaxies are randomly placed with the only conditions that (i) the minimum galaxy-galaxy distance is 40 pixels (ii) and the minimum galaxy-star distance is 60 pixels. Care is taken to distribute the centre of the galaxies randomly at the sub-pixel level: a uniform distribution of -0.5 to 0.5 from the centre (in both directions) is used. The star sub-patterns are separated by 2048 pixels in the serial direction and 2066 pixels in the parallel direction (for the nominal optical magnification). In each sub-pattern, the stars are arbitrarily placed (see Fig. 3) with different sub-pixel positions and slightly shifted horizontally and vertically with respect to each other to avoid cross-pollution by charge release trails.

The FWHM of the galaxies is uniformly distributed in the range 0.15-0.60 arcsec ([1.48, 5.94] pixels). The q-value of the galaxies (the ratio between the major and minor axes) is uniformly distributed between 0.3 and 1.0, i.e. between perfectly round galaxies (q=1) and moderately elliptical galaxies (q=0.3). The lower limit on the q-value is chosen to prevent the inclusion of extremely stretched galaxies. The orientation of the galaxy is random. The stars are circles with a radius of 0.03 arcsec (< 0.3 pixels).

2.4 Mask manufacture

The mask fabrication took place at Delta Mask B.V. (Enschede, The Netherlands) in a similar fashion as a lithographic mask; it consists in a deposited chromium layer on a quartz substrate, using 10×10 cm wafer with a thickness of 2.3mm.

The detailed description for each mask was specified in the GDSII file format. The GDSII specification does not contain elliptical shapes; the galaxies were thus approximated by polygons (up to about 200 sides depending on the galaxy size).
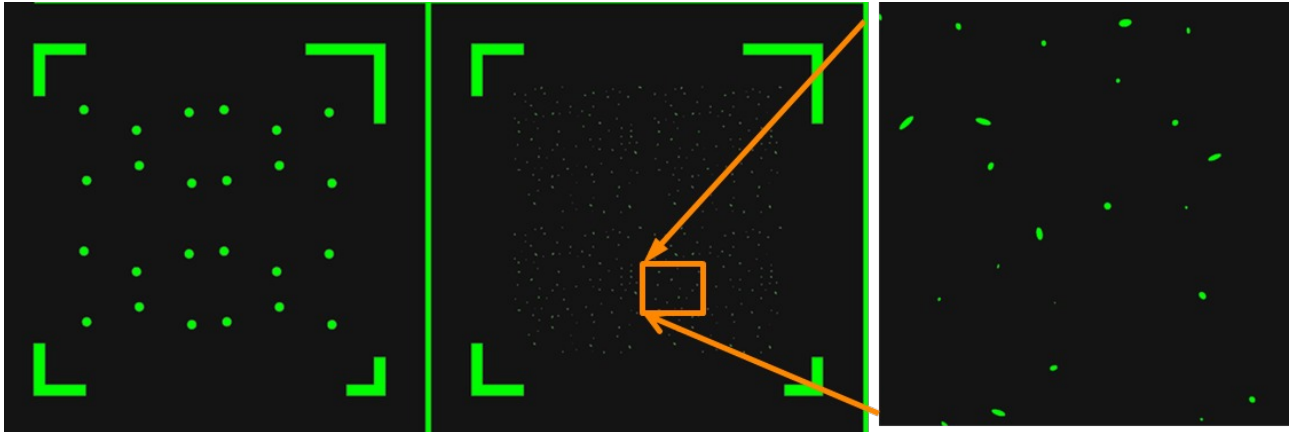
Figure 3. Mask pattern: the star locations are shown on the left and the galaxy distribution in the middle. A close up (right) gives a visual impression of the different galaxy sizes and shapes.

2.5 Optical setup and performance

The optical setup is described in Fig. 4. The main driver for the optical setup design is that the PSF properties must be as uniform as possible over the projection area to preserve the mask element properties (especially the shape) and that the Euclid VIS PSF FWHM is required to be smaller than 22 μm (~1.8 pixels). To obtain a rather constant PSF FWHM of 22 μm over an area of up to 3 cm∅, we use an EL-Nikkor 50 mm lens with a circular f/4 aperture.
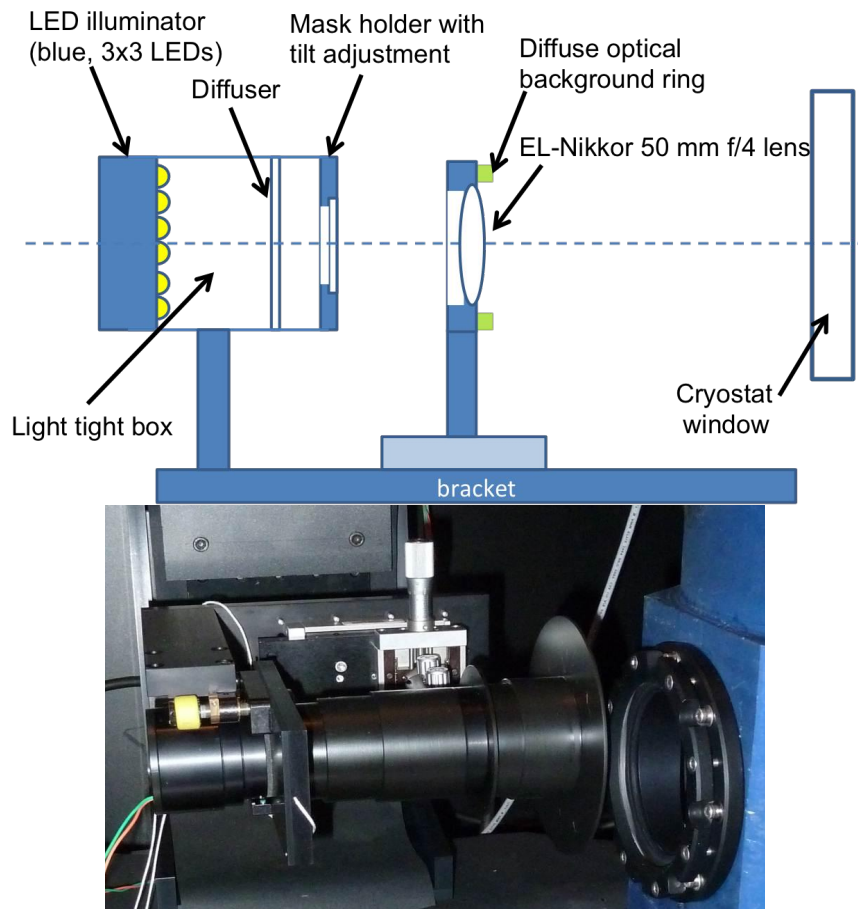

Figure 4. Schematic (top) and photograph (bottom) of the 3-axis translatable mask projection optical setup. On the photograph the setup includes including an extended enclosure to protect against stray light.

We achieve a PSF average size smaller than 1.6 pixels at best focus with uniformity over the mask area better than 0.1 pixels. The entire optical system is translated to project the mask over each CCD quadrant. The PSF properties over each quadrant are quasi-identical; this allows us to proceed with our experiment concept where identical mask elements are compared for images taken over different quadrants.

Using dithering we can reconstruct the average PSF shape for each of the four mask patterns over a single quadrant (shown in Fig. 5) and measure a significant spread in PSF ellipticity e from 0.05 to 0.15. This means that within the same quadrant, the same galaxy in the different sub-patterns has a different ellipticity; this prevents us from making strict comparison between sub-patterns (e.g., error measurement using a single image).
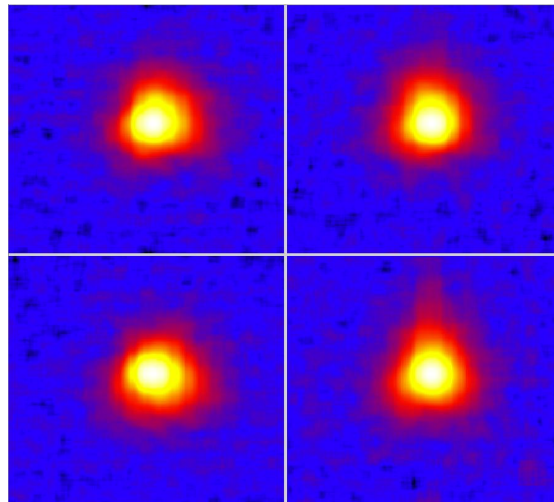

Figure 5. Reconstructed PSF at best focus for each mask corner (sub-pattern) including 6 stars each (the colour scale is logarithmic).

The surface presented to the light source is the substrate and not the metal to avoid any undesired light reflections. The light source is an array of (blue) LEDs emitting at $\lambda = 470$ with bandwidth 25 nm to minimize light coming through the chromium layer. A uniform diffuse optical background can be generated using a ring composed of an electro-luminescent material (Proto-Kut, Graphics Solutions International, LLC) located around the lens. During the experiment the number of collected photoelectrons is determined by the light source brightness, the mask opacity, the exposure time, and the size of the galaxy and star-like mask elements. The galaxy elements being larger than the star ones, they appear brighter than stars contrary to a realistic scene. An overlay mask can be used to block the galaxy light during integration to obtain a realistic scene with faint extended objects (galaxies) and bright point-like sources (stars). Results using this overlay mask are not presented here; we used in our analysis so far a simple moment-based method to determine the galaxy shapes, which does not require a local PSF determination (see Section 2.6).

2.6 Data acquisition and analysis steps

An acquisition sequence corresponds typically to a certain number of frames N obtained for each of the four mask positions (over quadrant E, F, G, H) using one signal level (i.e. one LED intensity and exposure duration) and one readout direction only (either the closest or the opposite readout node). E.g., when N frames are obtained for quadrant E, the optical setup is translated (automatically) to the next quadrant F and so on. At the end of this sequence a series of dark frames (i.e. LED turned off) is obtained following the exact same configuration: readout scheme and exposure duration. This is necessary to proceed to an accurate electronic offset removal. Generally from 100 to 200 frames were acquired per mask position per signal level and 40 dark frames were obtained for each data acquisition sequence

For each frame, we first carefully remove the electronic offset and then convert digital units into electrons (using conversion factors from previously measured photon-transfer curves). For each galaxy in the image (or more generally a

subset of them), we then determine the ellipticity: we apply a moment-based method including a weighting Gaussian function (σ_{gauss} = 7.42 pixels) on a 40×40-pixel window centered on the brightest pixel.

The residual background (stray light, chromium transparency) is measured to be less than one electron such that no background removal procedure is required, when the diffuse optical background source is turned off.

As already mentioned is Section 2.1, we repeat these steps for damaged and CTI-free images[*] and then compute the mean ellipticity for each galaxy as well as for each mask sub-pattern to infer the CTI-induced errors and bias.
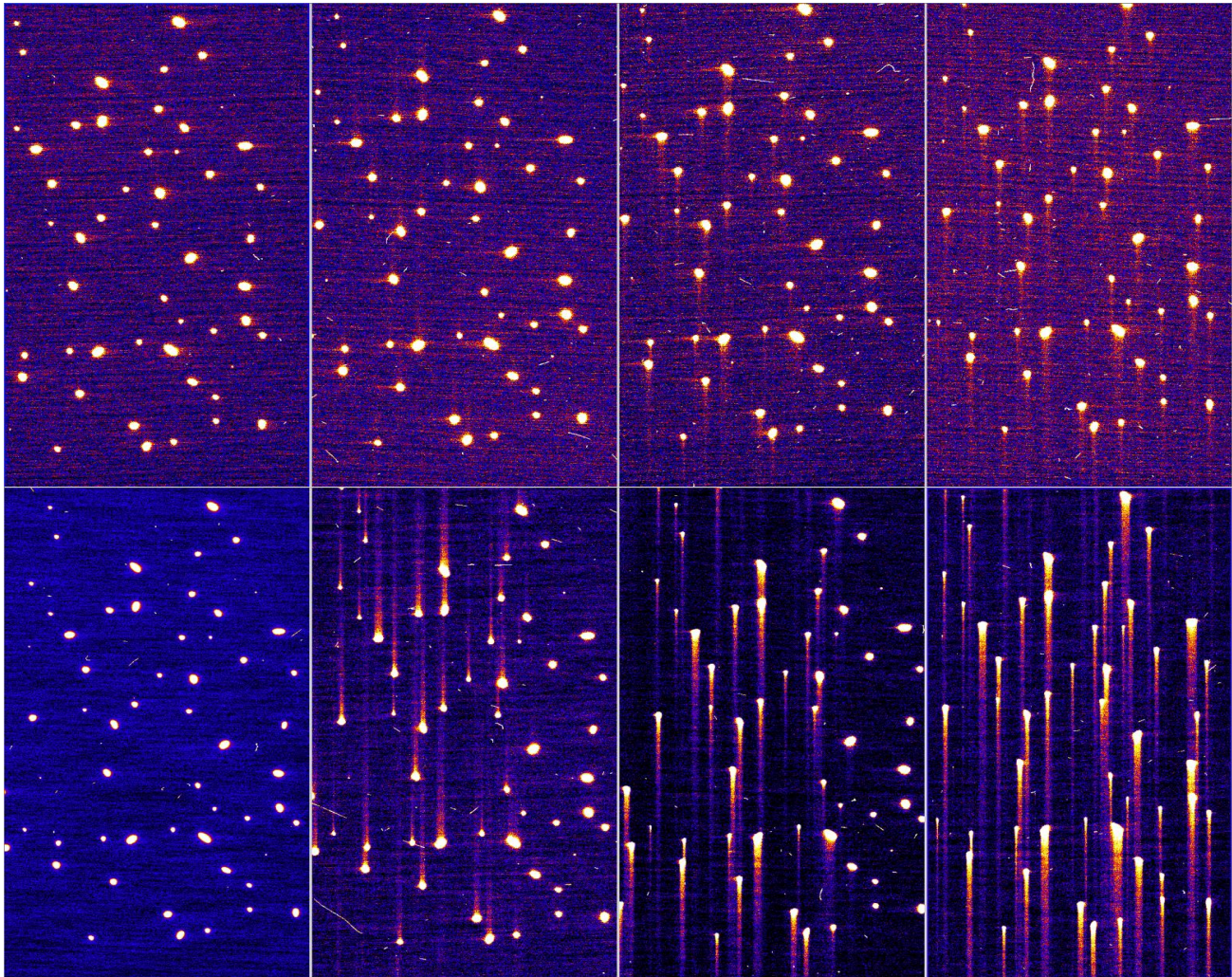
3. FIRST RESULTS

Figure 6. Close-up over the same mask region for a 100-image average at T= 153 K (top) and T = 173 K (bottom). From left to right each column corresponds to the different mask locations with readout through the closest output node: E (reference), F (eol/2), G (eol), H (eol, parallel CTI only). The vertical and horizontal directions correspond to respectively the parallel and serial transfer directions. The signal level corresponds to 14 ke- (the colour scale is logarithmic).

---

[*] CTI-free images do contain CTI – the CCD native CTI – that we ignore in our analysis.

We present the first results obtained using the setup and measurement concept described above. For conciseness, we focus exclusively in the following on the characterization of the CTI-induced errors $\overline{\delta_g}$ – in the form of ellipticity error maps – and bias $\left\langle\overline{\delta}\right\rangle$ in the ellipticity measurement. Note that the same data and methods can also be used to study other CTI-induced errors: photometric errors and the associated decrease in signal-to-noise (SNR) ratio due to charge loss, astrometric errors due to the image location shift, and other shape-measurement associated errors in galaxy size and orientation determination.

We distinguish between three cases: serial CTI only, parallel CTI only, and parallel and serial CTI combined. And we present results for two different signal levels: 14 and 140 ke$^-$ obtained using different LED intensity but the same 7 s-exposure duration. The signal level corresponds to the mean flux considering all the galaxies in one image. The flux for each galaxy is computed by summing over a 40×40-pixel window centered on the brightest pixel. These signal levels correspond roughly to 10 and 100 times the number of signal electrons expected for a galaxy with SNR 10 for a background of 72 e$^-$ pixel^{-1} at readout. Note however that no diffuse background was applied.

Figure 6 shows a qualitative impression for the 14 ke$^-$ signal level of the CTI-effects before and after irradiation at 153 K the nominal temperature of operation and 173 K. While no trailing can be distinguished for the non-irradiated quadrant in these operating conditions demonstrating excellent native-CTI performance, trails are clearly visible opposite to the parallel (vertical) and serial (horizontal) transfer directions for the irradiated quadrant. For the 173 K case, the parallel CTI is even more pronounced.
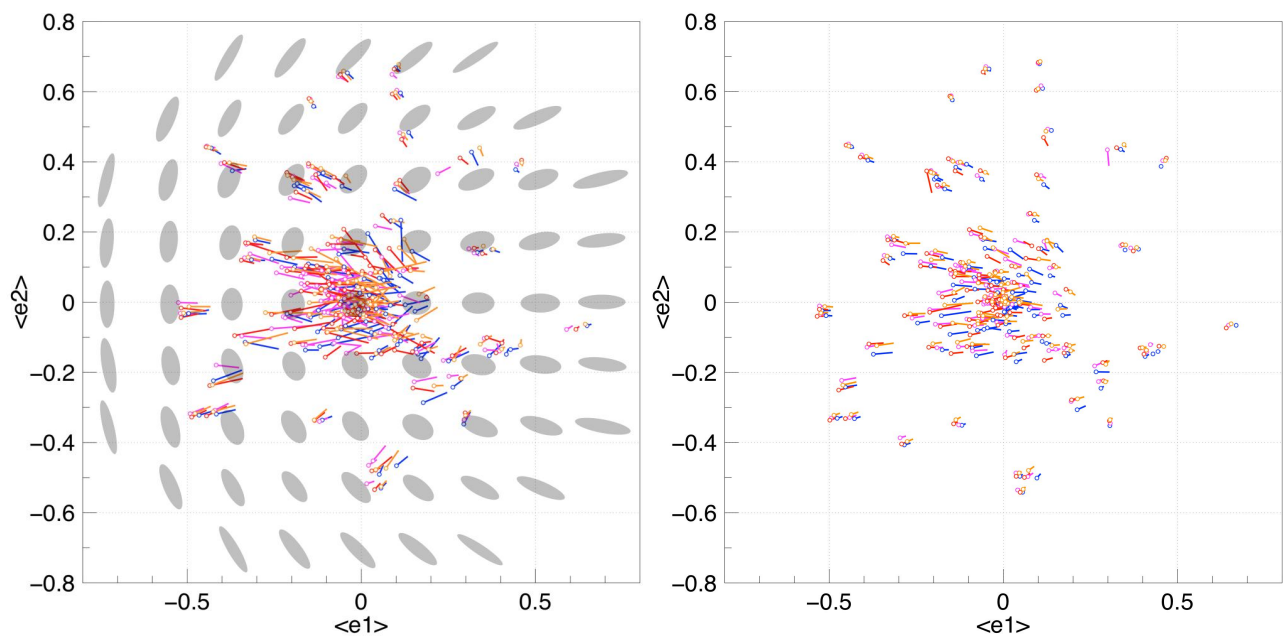
3.1 Serial CTI-induced errors

Figure 7. Serial-CTI ellipticity error maps for 14 ke- (left) and 140 ke- (right). The empty circle indicates the mean ellipticity over the CTI-free images for each of the 400 galaxies. The lines – error vectors – connect the mean ellipticity measured for the CTI-free images to the mean ellipticity measured for the damaged images. Each colour shows the results for galaxies that belong to a different mask sub-pattern (see Fig. 2). A very clear global shift towards greater e$_1$ is visible for both signal levels. The shift is more dramatic for lower signal levels. To facilitate the understanding of the ellipticity error maps, we draw in overlay schematic shapes at the corresponding to e$_1$ and e$_2$ values (left).

As shown in Fig. 2, by projecting the mask over one quadrant and reading out through the opposite node, it is possible to assess radiation-induced serial CTI and serial CTI only if one discards from the analysis the mask sub-patterns projected over the image-area irradiated regions. In quadrant F and G the serial register irradiated region corresponds to about 450 pixels. All 400 galaxies transfer through the same amount of irradiated pixels resulting in a rather clean measurement as can be observed from the ellipticity error maps shown in Fig. 7. We recall that e_1 is a measure of the galaxy elongation in the serial ($e_1>0$) and parallel ($e_1<0$) transfer directions, while e_2 measures the galaxy stretch in the same fashion but along axes oriented 45° away from the transfer directions (see the overlay schematic shapes in Fig. 7 left). As a result e_1 is expected to be the most affected by CTI.

A shift towards greater e_1 is indeed clearly visible (Fig. 7) especially for galaxies originally elongated in the parallel direction ($e_1<0$); as expected the charge trailing in the serial direction elongates galaxies in this direction and object already elongated in this direction ($e_1>>0$) are less affected by serial CTI. For e_2, the maps indicate a global shift (i.e. for both $e_2>0$ and $e_2<0$ galaxies) towards values closer to zero. For this reason we use the e_2 absolute values to compute a bias in e_2.

Table 1. Serial-CTI induced bias in ellipticity for different signal levels, radiation doses, and the two mask sub-patterns that do not suffer from parallel CTI. Note that these numbers correspond to 450 transfers through irradiated pixels.

Radiation dose	Mask sub-pattern	$\langle \delta_{e1} \rangle \pm \upsilon_{\langle \delta_{e1} \rangle}$	$\langle \delta_{|e2|} \rangle \pm \upsilon_{\langle \delta_{|e2|} \rangle}$
Signal level = 140 ke$^-$			
eol	1 (magenta)	-0.03816 ± 0.0002	-0.0006 ± 0.0002
eol	2 (red)	-0.03116 ± 0.0001	0.0019 ± 0.0002
eol/2	1	-0.01500 ± 0.0001	0.0020 ± 0.0001
eol/2	2	-0.01668 ± 0.0002	-0.0015 ± 0.0002
Signal level = 14 ke$^-$			
eol	1	-0.023 ± 0.002	0.065 ± 0.004
eol	2	-0.048 ± 0.001	0.025 ± 0.002
eol/2	1	-0.033 ± 0.001	0.005 ± 0.002
eol/2	2	-0.038 ± 0.002	0.024 ± 0.003

Table 1 lists the serial-CTI induced bias in e_1 and e_2. As expected the bias in e_1 is negative, as serial CTI elongates the galaxy in the serial direction inducing a greater e_1.

For bright signal levels the e_1 bias is of the order of several percent, and scales linearly with radiation dose. A difference at the 0.5% level can be noted between the biases in e_1 measured for two different mask sub-patterns. This is likely due to the PSF non-uniformity (in ellipticity/shape) over one CCD quadrant (Fig. 5).

For the 14 ke$^-$ signal level, the bias increases by at most a factor 2.5 (for eol/2) and the bias statistical uncertainty by a factor 10. However for the mask sub-pattern 1 and the eol radiation dose, we notice an unexpected drop in e_1 bias pointing towards extra uncertainties in our measurement not encompassed by the quoted statistical uncertainty (Eq. 3 and 4). This is further confirmed by the break in linearity with radiation dose at lower signal level.

The bias values for e_2 are at least an order of magnitude less than for e_1. For the lowest signal level, the e_2 bias dramatically increases. We attribute this increase to outliers (e.g., cosmic rays) not yet properly handled in our analysis.

3.2 Parallel CTI-induced errors

Figure 8 shows ellipticity errors computed using damaged images obtained by projecting the mask over the H quadrant (for which the serial register was not irradiated) and reading out through the H output node. The different colours show these errors for the different mask sub-patterns. Only sub-pattern #1 and #2 were projected over the image area irradiated region. Table 2 lists the measured e_1 and e_2 bias values for the two signal levels investigated.

For both signal levels, we note that the measured bias in e_1 for sub-pattern #1 is greater than for sub-pattern #2 by a factor of about 4. This is expected since the number of transfers through irradiated pixels depends now on the galaxy positions in the image area, contrary to the previous section. Given that the parallel size of the irradiated region in quadrant H is of about 1,500 pixels, one can roughly estimate that the average number of transfers through irradiated pixels for sub-pattern #1 and #2 are respectively 1,125 and 375 (factor 3). The deviation from the expected factor 3 is explained by the fact that the irradiated region is located closer to the CCD center than the serial register.
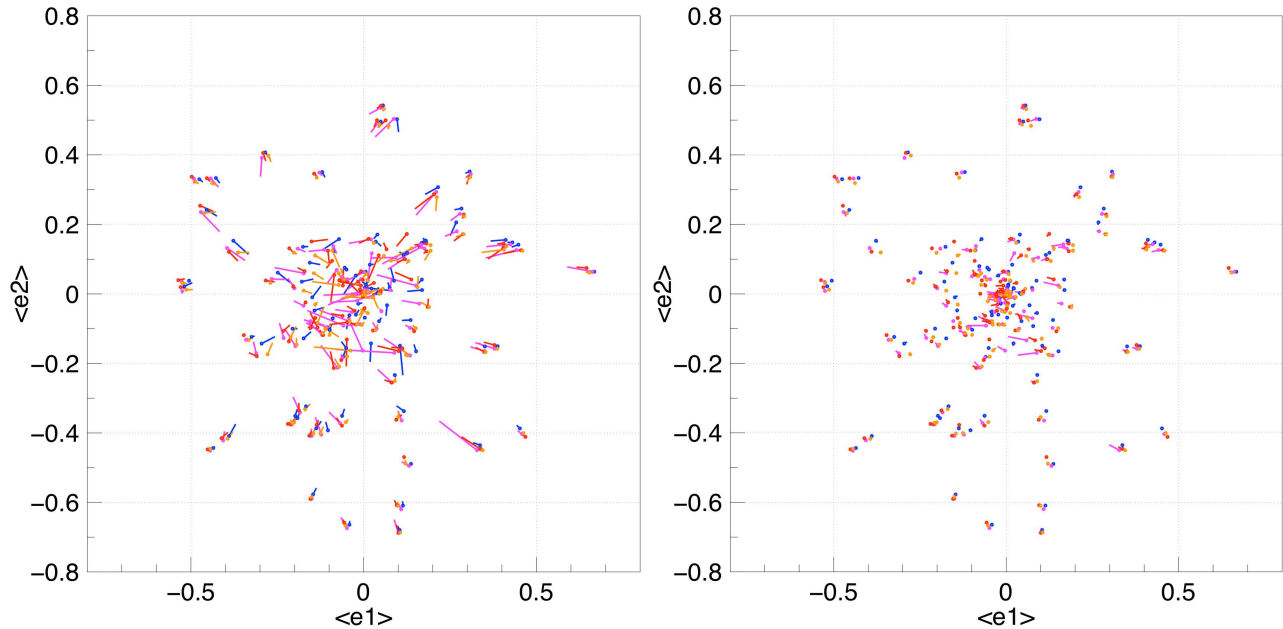

Figure 8. Parallel-CTI ellipticity error maps for 14 ke- (left) and 140 ke- (right). As shown in Fig. 2, only the mask sub-patterns #1 (magenta) and #2 (red) were projected over the image area irradiated region of quadrant H and as can be seen more clearly for the highest signal level (right), magenta and red vectors are the only one that can be distinguished from the empty circle showing the galaxy CTI-free ellipticity.

The bias values (Table 2) are positive as parallel CTI elongates the galaxies in the parallel direction ($e_1 < 0$). For the 14 ke- signal level, the bias increases by at most a factor 3.5. Although the bias in e_2 measured over the irradiated region (sub-patterns #1 and #2) is greater than for the one measured over the control region (#0 and #3), it does not scale with the number of transfers.

Monitoring the errors for #0 and #3 (projected over the quadrant H control region) enables the assessment of the non-CTI spurious ellipticity introduced in our measurement. As shown in Fig. 9 (blue and orange dots and lines) and listed in Table 2, the level of non-CTI spurious ellipticity measured for the highest signal level is very low ~0.05%. For e_1, the apparent increase at low signal level is compensated by a lower measurement precision. For e_2, the increase is more severe and should be further investigated.

Table 2. Ellipticity bias for different signal levels and mask sub-patterns; only the sub-patterns #1 and #2 suffers from parallel CTI.

Radiation dose	Mask sub-pattern	$\langle \delta_{e1} \rangle \pm \upsilon_{\langle \delta_{e1} \rangle}$	$\langle \delta_{|e2|} \rangle \pm \upsilon_{\langle \delta_{|e2|} \rangle}$
Signal level = 140 ke⁻			
Control region	0 (blue)	0.0005 ± 0.0001	0.0004 ± 0.0002
eol	1 (magenta)	0.0129 ± 0.0001	0.0029 ± 0.0001
eol	2 (red)	0.0027 ± 0.0001	0.0030 ± 0.0001
Control region	3 (orange)	-0.0006 ± 0.0001	0.0005 ± 0.0002
Signal level = 14 ke⁻			
Control region	0	-0.0014 ± 0.0008	-0.011 ± 0.001
eol	1	0.0368 ± 0.0008	0.004 ± 0.001
eol	2	0.0095 ± 0.0008	-0.008 ± 0.002
Control region	3	0.001 ± 0.001	-0.014 ± 0.002

3.3 Parallel and serial CTI-induced errors

Finally we measure the ellipticity errors for galaxies affected by both parallel and serial CTI. We compare results obtained for quadrant F (eol/2) and G (eol) for which both image area and serial register were irradiated. We focus on the mask sub-patterns located the furthest away from the output node #3 and #0 for F and G respectively.
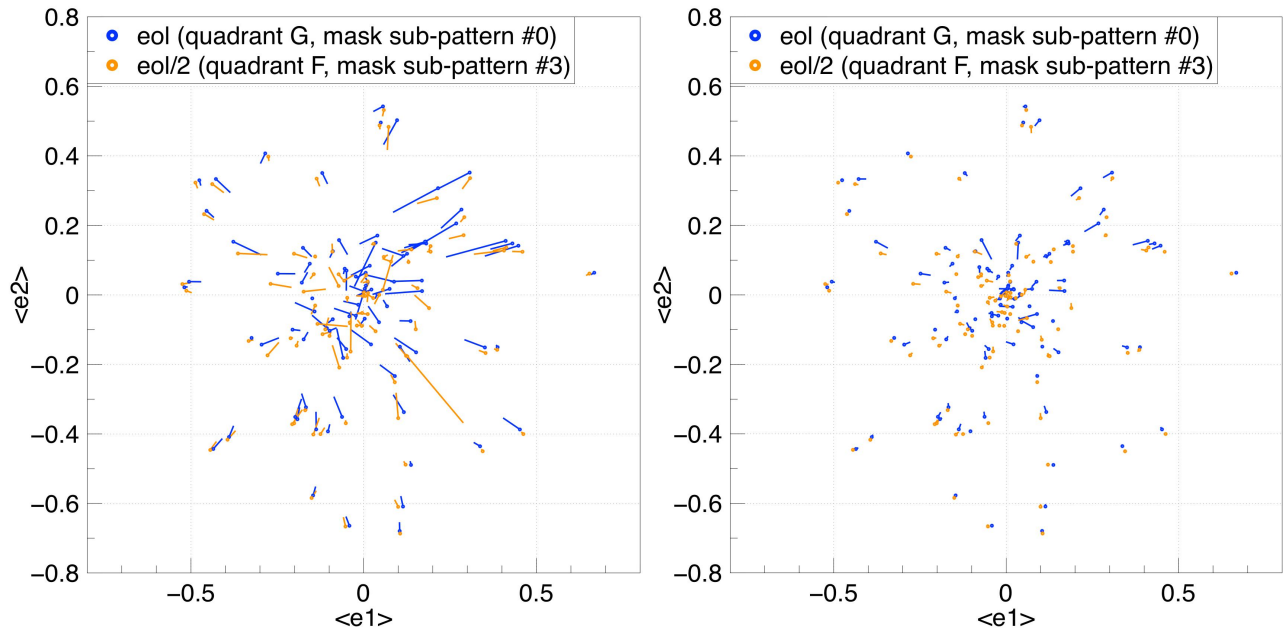

Figure 9. Combined parallel and serial CTI ellipticity error maps for 14 ke⁻ (left) and 140 ke⁻ (right). We show the results obtained for the mask sub-patterns projected the furthest away from the output node: #3 for quadrant F (eol/2) and #0 for quadrant G (eol). For both e_1 and e_2 one can observe a clear shift towards values close to zero. This effect is much more pronounced at smaller signal levels.

Figure 9 shows the resulting error maps for the two signal levels (left, right) and two radiation doses: eol (blue) and eol/2 (orange). As demonstrated in the previous sections, parallel CTI shifts the e_1 distribution towards negative values and serial CTI towards positive values. However parallel CTI affects primarily galaxies with shapes elongated in the serial direction ($e_1>0$) and serial CTI affects primarily shapes elongated in the parallel direction ($e_1<0$). This effect is illustrated in Fig. 9 where most error vectors point towards zero.

Due to the same effect, the measure e_1 bias values (not listed here) are lower than in the serial CTI and parallel CTI only cases. Similar e_2 bias values are measured.

4. DISCUSSION

For the highest radiation dose and lowest signal level measured, we found a maximum serial-CTI induced bias in e_1 of -0.048 for 450 transfers and a maximum parallel-CTI induced bias of 0.0368 for 1,125 transfers. We can extrapolate these measurements to a worst-case scenario: radiation dose at end of mission (eol) and a maximum number of either or both serial and parallel transfers of about 2,000, as well as to a 'mean' scenario: radiation dose accumulated halfway through the mission (eol/2, this may not be accurate depending on the launch date and the solar cycle) and a mean number of transfers of about 1,000. The worst-case scenario gives a maximum CTI-induced bias in e_1 of -0.21 for serial CTI, and 0.07 for parallel CTI, the mean scenario gives respectively -0.05 and 0.02. For comparison, based on simulations, the values assumed during the Euclid study phase [7] (including zodiacal light background) for a worst-case scenario ranged from 0.05 to 0.02: a factor 4 lower than our measured values and closer to our mean scenario. Parallel CTI was assumed to be a factor 2 worse than serial CTI, while we find serial CTI is a factor-3 greater than parallel CTI.

This is before any correction at the image processing level is applied. After correction the residual contribution of CTI to the ellipticity of the system PSF is required to be less than 1.1×10^{-4} per VIS exposure per ellipticity component (i.e. e_1 or e_2) [8, 9]. The measured values confirm the need for a very efficient CTI software mitigation procedure. The Euclid red book study [7] mentions that for our mean-scenario bias values it is theoretically possible to recover the expected ellipticity measurement accuracy using a correction algorithm similar than for HST [10].

Note also that values quoted in [7] correspond to SNR 10 galaxies that is a signal level 10 times lower than the lowest signal level measured in our study; a greater discrepancy between actual measurement and simulation is to be expected. However it is important to list here, our experiment uncertainties and differences between our experiment and the real VIS operation and Euclid shape measurements that may influence the presented results and conclusions.

With respect to our experiment uncertainties, Section 3 shows that despite identifiable trends in the ellipticity error maps (Fig. 7, 8, 9) the ellipticity bias measurement show a greater scatter than the computed statistical uncertainty (Table 1 and 2), and – at lower signal level - break in linearity with respect to the number of transfers or radiation dose. This calls for refinements in our analysis in particular the outlier rejection procedure.

The greatest difference between our experiment and the in-orbit CCD operation and environment is the absence of light background (72 to 90 e^- pixel^{-1} at readout). During operation the background light is expected to permanently fill a fraction of the traps with the longest release time constant. However this is expected to affect mostly parallel CTI only, which did not show the greatest impact on the ellipticity bias. As shown in Fig. 4, a diffuse optical background ring has been implemented, and a new set of data will be acquired soon to test the previous hypothesis. Our shorter 7 s-exposure duration (instead of 565 s) may lead to underestimate parallel CTI, while the use of a less elaborate and non-optimized parallel clocking scheme than currently envisaged leads to overestimate parallel CTI. We test the impact on measured CTI of some of this clocking and exposure duration aspects in [2]. Anyhow this is again not affecting serial CTI that is the greatest contributor to the measured ellipticity bias.

Finally we used a very simple moment-based shape measurement not optimized against CTI. A more complex moment-based method with tunable weighting function (e.g. wrt to the galaxy size etc.) or a forward modelling approach may give less severe results. However we consider these methods belonging to the set of potential CTI software mitigation procedures that shall be tested in a second step using the same data we have presented.

5. CONCLUSIONS AND FUTURE WORK

We designed an experiment to measure and proceed to a model-free characterization of the errors introduced by radiation-induced CTI in the Euclid galaxy shape measurement. We detailed the experiment concept and current implementation as well as the first results obtained for an irradiated Euclid prototype CCD operated in close-to Euclid-like conditions. Our measurement concept consists in monitoring the change in ellipticity between the same mask elements projected over irradiated and reference regions of the tested CCD. This relies on the assumption that the optical system ellipticity remains the same for different mask projection locations. We are able to test this assumption using control regions in the irradiated CCD quadrants. We measure that the level of spurious ellipticity introduced by non-CTI effects in our measurement is an order of magnitude less than the smallest CTI-induced measured spurious ellipticity, close to the measurement precision.

We can disentangle between serial and parallel CTI and present our results for three different cases: serial CTI only, parallel CTI only, and combined parallel and serial CTI. Each case corresponds to a realistic scene with a different galaxy image location on the CCD: respectively, the galaxy image is located close to the CCD serial register but away from the output node, close to the output node but away from the serial register, and furthest away from both the serial register and output node. We present ellipticity error maps and list bias values as a function of two signal levels and radiation doses. As expected our measurements show that e1 is the most affected ellipticity component and the CTI errors depend on the galaxy original orientation and shape. We find that the serial-CTI induced bias (computed for a set of galaxies with different orientation, size, shape) in the first ellipticity component – e_1 – is roughly a factor three greater than the parallel-CTI one, contrarily to previous simulations used during the Euclid definition phase. Extrapolating our results, we find that the bias introduced in e_1 for the greatest amount of transfer possible is -0.21 for serial CTI, and 0.07 for parallel CTI – a factor 4 greater than the worst-case scenario envisaged during the Euclid definition phase. This is before any correction is applied at the image processing level. According to the Euclid requirements, after correction the residual ellipticity bias introduced by CTI should be less than 0.00011. This study results thus reaffirm the need for an efficient CTI mitigation scheme in the Euclid data processing.

Our measurements at high signal levels show the expected linear increase of the CTI effects on the ellipticity measurement with radiation dose and the number of charge transfers. At lower signal level the CTI effects clearly increase, so does the uncertainty in our measurement: despite trends still clearly identifiable in the ellipticity error maps, we note that the measured bias deviates from the linearity observed at higher signal levels. This indicates we need to refine our analysis in particular the handling of outliers introduced by for instance cosmic rays.

Finally we discussed how representative our experiment is considering the current clocking scheme envisaged for the Euclid CCDs and the in-orbit operation of the VIS instrument. To be as realistic as possible we need to repeat our measurements at lower signal levels (one order of magnitude) including a diffuse optical background.

The current data will be made available to the Euclid consortium to test and refine the different solutions to calibrate for CTI in the Euclid data processing during or prior to the galaxy shape measurement.

REFERENCES

[1] Short, A. D. T. et al., "The Euclid VIS CCD detector design, development, and programme status," Proc. SPIE 9154-2, (2014).

[2] Prod'homme, T. et al., "A comparative study of charge transfer inefficiency value and trap parameter determination techniques making use of an irradiated ESA-Euclid prototype CCD," Proc. SPIE 9154-33, (2014).

[3] Murray, N.J., et al. "Multi-level parallel clocking of CCDs for: improving charge transfer efficiency, clearing persistence, clocked anti-blooming, and generating low-noise backgrounds for pumping," Proc. SPIE. 8860, (2013).

[4] Verhoeve, P. et al., "CCD characterisation for space missions at ESA," Proc. SPIE 9154-15 (2014).

[5] Verhoeve, P. et al., "ESA's CCD test bench for the Euclid visible channel," Proc. SPIE 8453-22, (2012).

[6] Cropper, M. et al., "VIS: the visible imager for Euclid," Proc. SPIE 9143-18, (2014).

[7] Laureijs, R. et al., "Euclid Definition Study Report, " [eprint arXiv:1110.3193], (2011).

[8] Massey, R. et al., "Origins of weak lensing systematics, and requirements on future instrumentation (or knowledge of instrumentation)," MNRAS, (2013).

[9] Cropper et al., "Defining a weak lensing experiment in space," MNRAS, (2013).

[10] Massey, R. et al., "An improved model of charge transfer inefficiency and correction algorithm for the Hubble Space Telescope," MNRAS, (2014).